Electrochimica Acta 476 (2024) 143673

Contents lists available at ScienceDirect

Electrochimica Acta

journal homepage: www.journals.elsevier.com/electrochimica-acta

Zn-doped Cr_2O_3 oxides boosted the electrochemical performance of aqueous hybrid supercapacitor

Tianyang Fei[a,1], Tauqeer Ahmad[b,1], Muhammad Usman[c], Awais Ahmad[d,*], Adil Saleem[e], Muhammad Bilal Hanif[f], Abdulnasser M. Karami[g], Muhammad Sufyan Javed[h], Bhargav Akkinepally[i,*], Changlei Xia[a,*]

[a] College of Materials Science and Engineering, Nanjing Forestry University, Nanjing, Jiangsu 210037, China
[b] Department of Chemical and Biological Engineering, University of Porto, Faculty of Engineering, Rua dr. Roberto Frias, 4200-465 Porto, Portugal
[c] Department of Metallurgical and Materials Engineering, University of Porto, Faculty of Engineering, Rua dr. Roberto Frias, 4200-465 Porto, Portugal
[d] Department of Chemistry, The University of Lahore, Lahore, 54590, Pakistan
[e] Department of Mechanical, Materials and Aerospace Engineering, Illinois Institute of Technology, Chicago, IL 60616, United States
[f] Department of Inorganic Chemistry, Faculty of Natural Sciences, Comenius University in Bratislava, Ilkovicova 6, Mlynska Dolina, 842 15, Bratislava, Slovakia
[g] Department of Chemistry, College of Science, King Saud University, Riyadh 11451, Saudi Arabia
[h] School of Physical Science and Technology, Lanzhou University, Lanzhou 730000, China
[i] School of Mechanical Engineering, Yeungnam University, Daehak-ro, Gyeongsan-si, Gyeongbuk-do 38541, South Korea

ARTICLE INFO

Keywords:
$ZnCr_2O_4$
Binder-free
Zn-doping
Aqueous hybrid supercapacitor

ABSTRACT

Aqueous hybrid supercapacitors (AHSCs) have emerged as a promising choice for advanced energy storage systems in the next generations. It is primarily due to their exceptional characteristics, such as superior power density, non-flammability, and environmental compatibility. However, compared to non-aqueous supercapacitors, the small working potential windows and less cycle stability are their key challenges to solve. A facile method was used to synthesize Zn-doped Cr_2O_3 supported on carbon cloth (CC) as a binder-free electrode for AHSCs and denoted as $ZnCr_2O_4$@CC. According to the experimental findings, the $ZnCr_2O_4$@CC material possesses a rapid charge transfer. As a result, the $ZnCr_2O_4$@CC electrode showed a remarkable charge storage performance with dominant charge storage by capacitive type (68.4 % at 10 mVs^{-1}). Further, the $ZnCr_2O_4$@CC electrode exhibits a maximum capacitance of 374 Fg^{-1} at 1 Ag^{-1} and outperforms its counterparts (194 Fg^{-1} for Cr_2O_3 and 60.78 Fg^{-1} for ZnO). After 10,000 cycles, the $ZnCr_2O_4$@CC electrode still shows 98.1 % of its initial capacitance, demonstrating its potential for practical applications. The AHSC device also constructed using $ZnCr_2O_4$@CC as a cathode and activated carbon (AC) as an anode with 1 M KOH as an electrolyte ($ZnCr_2O_4$@CC//AC-AHSC). The AHSC device exhibits an excellent capacitance retention of 96.43 % after 10,000 cycles. Further, the AHSC shows a superb energy density of 26.2 $Whkg^{-1}$ at a power density of 800.6 Wk¯1 g. The current work describes a new strategy for the production of next-generation aqueous hybrid supercapacitors with exceptional electrochemical performance.

1. Introduction

The global energy use is rising rapidly due to the fast growth of electronics and a growing population [1–3]. The existing possibilities for generating energy from winds, solar, and various other renewable sources such as nanogenerators are incorporating to meet the continuously growing energy need [4–6]. In addition, most of these methods of producing or transforming energy are inconsistent; hence, appropriate storage systems are essential to work effectively as an alternative to fossil fuels with carbon free and environmentally friendly [7–9]. Significant investigations over the past few decades have been prompted by this phenomenon, leading to the development of today's electrochemical energy devices, including energy storage devices such as lithium-ion batteries [10,11], and energy conversion devices such as solar cells [12,13]. Due to the harmful nature and low power density of lithium-ion batteries; new energy storage technologies have been

---

* Corresponding authors.
E-mail addresses: awaisahmed@gcuf.edu.pk (A. Ahmad), bhargav@ynu.ac.kr (B. Akkinepally), changlei.xia@njfu.edu.cn (C. Xia).
[1] Contributed as equal first author.

https://doi.org/10.1016/j.electacta.2023.143673
Received 18 August 2023; Received in revised form 2 December 2023; Accepted 14 December 2023
Available online 15 December 2023
0013-4686/

emerged such as dual ion aqueous batteries [14–16]. At the same time other energy storage technologies also under investigation based on the multivalent ion storge such as aluminum [17], calcium [18] and zin-ion batteries [19]. However, the rate performance and long-term cycling stability of these devices are still unsatisfactory. Recently, supercapacitors (SCs) have garnered significant attention as a promising energy storage technology owing to their notable characteristics, including a high-power density, extended operational lifespan, and rapid charging rate [20,21]. Aqueous hybrid supercapacitors (AHSCs) have attracted considerable attention owing to their cost-effectiveness, exceptional stability, and environmentally sustainable nature [22]. Nevertheless, the challenge persists in developing electrode materials that are highly efficient for SCs, particularly for AHSCs. Numerous materials have been subject to investigation, revealing that a significant number of them exhibit either a high energy density or a high-power density, but not both simultaneously.

Transition metal oxides (TMOs) have been investigated as potential electrode materials for energy storage applications [23]. Among the various TMOs, Cr_2O_3 is an attractive choice due to its notable theoretical capacitance and stability. Cr_2O_3 exhibits a variable oxidation state and possesses several desirable properties, including cost-effectiveness, favorable chemical stability, high thermal stability, excellent cyclability, and widespread accessibility. Consequently, it emerges as a promising candidate for SCs [24–27]. For instance, Shafi et al. [28] synthesized the ultrafine Cr_2O_3 particles and studied the structural and electrochemical properties. Specifically, they demonstrated a specific capacitance of 340 Fg^{-1} at 0.5 Ag^{-1}, with 85 % of their initial capacitance retained after 3000 cycles. Xu et al. [29]. reported that $NiCr_2O_4$ nanoparticles are an electrode material for SCs. The specific capacitance of $NiCr_2O_4$ in three-electrode systems is 422 F/g at a current density of 0.6 A/g. However, the specific capacitance is low to meet the needs of the actual applications. Recently, Zhang et al. [30]. reported that the $NiCrO_3$@CC electrode possessed a high capacitance of 2862 F/g at 1 A/g with an excellent cycling stability of 98.3 % after 10,000 cycles at 10 A/g. The synergistic effect of nickel and chromium ions promotes the rapid progression of redox reactions, providing high specific capacitance and high cycling stability. Nevertheless, due to its inadequate conductivity, Cr_2O_3 does not exhibit favorable characteristics as a potential electrode material in SCs. To address the limitation, the introduction of metal ions as dopants has been suggested to improve the electrochemical features of Cr_2O_3-based electrodes. Furthermore, the process of doping results in a substantial increase in carrier concentration through the generation of free-charge carriers [31]. Recent research has demonstrated that doping with extrinsic impurities like Cu, Mn, Zn, and B improves materials' electrical, magnetic, and electrochemical properties [32]. The incorporation of Zn as a dopant can be an effective method for enhancing the electrochemical characteristics of diverse materials employed in energy storage systems. Its ability and low cast to improve surface area and stability render it a promising strategy for advancing more efficient and practical energy storage technologies.

Moreover, Cr_2O_3 exhibits exceptional stability when subjected to different working conditions. Due to its intrinsic chemical and thermal stability, it exhibits a high level of resistance to deterioration, even in severe conditions. This consistency is especially beneficial in situations where long-term performance and durability are crucial [33]. Cr_2O_3 has several noteworthy advantages, other from its capacity and stability. For example, it demonstrates excellent conductivity, which is essential in applications that need efficient charge transfer or electron transport [34]. This feature facilitates improved performance and overall efficiency of the energy storage system. Furthermore, Cr_2O_3 is abundant on earth, economically viable, and ecologically sustainable, rendering it a compelling substitute for other elements that may be rare or environmentally harmful.

Herein, a facile hydrothermal method was employed to synthesize binder-free Zn-doped Cr_2O_3 supported on carbon cloth. According to the experimental results, the $ZnCr_2O_4$@CC electrode showed a remarkable charge storage performance with dominant charge storage by capacitive type (68.4 % at 10 mVs^{-1}). Further, the $ZnCr_2O_4$@CC electrode exhibits a maximum capacitance of 374 Fg^{-1} at 1 Ag^{-1} and outperforms its counterparts (Cr_2O_3 and ZnO). After 10,000 cycles, the $ZnCr_2O_4$@CC electrode still shows 98.1 % of its capacitance, demonstrating its potential for use in the developing field of renewable energy. The AHSC device was also constructed using $ZnCr_2O_4$@CC as a positive electrode and activated carbon as a negative electrode with 1 M KOH (denoted as $ZnCr_2O_4$@CC //AC-AHSC). The AHSC device exhibits excellent capacitance retention of 96.43 % after 10,000 cycles with high energy and power densities.

2. Experimental method

2.1. Synthesis of $ZnCr_2o_4$@CC

$ZnCr_2O_4$@CC was successfully synthesized using a simple and efficient hydrothermal technique. Typically, 1.5 g of $Zn(NO_3)_2$, 2.5 g of Cr (NO3), 0.5 g of NH_4F, and 2.5 g of CH_4N_2O were dissolved in 50 mL of deionized (DI) water by stirring the solution for 30 min. The solution was then placed in an autoclave and heated at 150 °C for 24 h. After cooling, the $ZnCr_2O_4$ precursor at CC was washed three times with deionized water and once with ethanol and dried at 60 °C for 12 h [35]. To convert the precursor into crystalline $ZnCr_2O_4$@CC, the sample was annealed in an air environment at 600 °C for 2 h. Subsequently, the $ZnCr_2O_4$@CC was employed for subsequent analytical examination and evaluation of its electrochemical properties. The synthesis of Cr_2O_3 and ZnO, the same procedure was employed using the relevant raw materials.

2.2. Physical characterization

The material's morphology was studied using a field emission scanning electron microscope (FESEM, HITACHI SU8220), a transmission electron microscope (TEM, FEI Themis Z), and an energy-dispersive X-ray spectrometer. The sample's elemental composition was studied using X-ray photoelectron spectroscopy (XPS).

2.3. Electrochemical characterization

The as-synthesized $ZnCr_2O_4$ was used to prepare the working electrode. The slurry was prepared by homogeneously mixing the 80 % active materials, 10 % carbon black, and 10 % PVDF binder. The as-prepared slurry was cast on the carbon cloth on the area of 1 × 1 cm^2, and the mass loading densities was in the range of 1–1.5 mg cm^{-2}. In the three-electrode configuration, a platinum wire was employed as a counter electrode, and an Ag/AgCl was used as a reference electrode in 1 M KOH aqueous electrolyte. The galvanostatic charge-discharge (GCD), cyclic voltammogram (CV), and electrochemical impedance spectroscopy (EIS) were measured using an electrochemical workstation (CHI 660E, China). The CV tests were conducted in a voltage window of −0.5 to 0.1 V; GCD tests were carried out in the range of 1–20 Ag^{-1}, and EIS was tested in the frequency range of 0.001 to 100 kHz. For AHSC device, the positive electrode (cathode) was the same as above for the three-electrode configuration, and the negative electrode (anode) was based on the AC supported on CC and 1 M KOH aqueous electrolyte in a coin cell system. The coin cells were designed in the presence of a separator, Whatman filter paper.

2.4. Calculations

The single electrode's capacitance (C_{sp} (Fg^{-1}) and AHSC device's capacitance C_d (Fg^{-1}), power density (P) (Wkg^{-1}), and energy density (E) ($Whkg^{-1}$) are all computed as follows:

$$C_{sp} = \frac{I\Delta t}{m \times \ \Delta V} \tag{1}$$

$$C_d = \frac{I\Delta t_d}{M \times \ (V)} \tag{2}$$

$$E = \frac{1}{2} C_d V^2 \times \frac{1000}{3600} \tag{3}$$

$$P = \frac{E}{\Delta t} \tag{4}$$

Where, Δt(s) denotes the discharge time, I(A) represents the current, m (g) reveals the mass of active material for three-electrode configuration, M(g) shows the mass of both cathode and anode in the AHSCs, and V(V) denotes the voltage window.

3. Results and discussion

Fig. 1 shows a schematic representation of the synthesis process $ZnCr_2O_4$ through a hydrothermal technique and a post-heat treatment in an air atmosphere. The precursor The next step was to produce a mechanically robust and crystalline material by annealing $ZnCr_2O_4$@CC for 2 h at 600 °C in an air environment. This strategy involves the preparation of $ZnCr_2O_4$ powder and then coating on the CC via the slurry casting method.

The morphology of the prepared samples was examined using FESEM and TEM. The FESEM image of ZnO revealed a nanosheet-like morphology composed of sharp needles with cross-linking, as shown in Fig. 2a. Similarly, Fig. 2b displays the sponge-like morphology of Cr_2O_3. In addition, Fig. 2c displayed the FESEM image of $ZnCr_2O_4$, which depicted the final morphology of nanosheets. The nanosheets have the potential to contribute to a higher surface area, increased electrochemical activity, and the development of extra charge storage sites with pseudocapacitive characteristics. The TEM further investigated the distribution of Zn inside the Cr_2O_3 matrices. A low-resolution TEM image (Fig. 2d) shows the homogeneous dispersion of Zn in Cr_2O_3, like the aforementioned FESEM results. Further, the intermediate resolution TEM image shows the sponge-like morphology of $ZnCr_2O_4$@CC (Fig. 2e). It facilitates the fast transfer of charge across interfaces and increases electrolyte ion accessibility to active sites. Additionally, $ZnCr_2O_4$ has a surface with large pores, which allows quick ion mobility and can enhance the electrochemical performance of the electrode. Further, a clearly lattice fringe can be seen in the high-resolution TEM image with an interplanar spacing of 0.243 nm, which corresponds to the (400) plane of $ZnCr_2O_4$ (Fig. 2f). The selected area electron diffraction (SAED) confirms the interplane spacing of 0.243 nm corresponding to the (400) index of $ZnCr_2O_4$ crystal structure (inset of the Fig. 2f) Furthermore, Fig. 2g displays the energy dispersive X-ray spectroscopy (EDS) of $ZnCr_2O_4$, providing evidence of the homogeneous distribution of all the elements. The elemental maps of Zn, Cr, and O confirmed the presence of Zn, Cr, and O elements, thereby indicating the successful formation of $ZnCr_2O_4$.

The successful preparation of ZnO, Cr_2O_3 and Zn-doped sample Cr_2O_3 samples was verified by room-temperature powder X-ray diffraction (XRD) as shown in Fig. 3a. All diffraction peaks are indexed according to the standard JCPDF numbers ($ZnCr_2O_4$:73–1962, ZnO: 89–0510 and Cr_2O_3: 84–0315). The sharp and intense peaks confirm the well crystalline nature of all samples without any impurity peaks.

Fig. 3b displays the high-resolution XPS spectrum for the Zn-2p orbital of the ZnO and $ZnCr_2O_4$ samples. The two distinct peaks observed at binding energies of 1020.1 and 1043.2 eV correspond to $2p_{1/2}$ and $2p_{3/2}$, respectively. The binding energy shows a little shift following $ZnCr_2O_4$ formation, from 1020.1 to 1019.5 eV for Zn-$2p_{3/2}$ and from 1043.2 to 1042.6 eV for Zn$2p_{1/2}$ lines, respectively, showing that the environment of Zn^{2+} at the surface is altered. Further, Fig. 3c displays the high-resolution XPS spectra of Cr-2p of the Cr_2O_3 and $ZnCr_2O_4$ samples. For the sample of Cr_2O_3, the two states of Cr-$2p_{3/2}$ and $2p_{1/2}$ were reported to have binding energies of 576.5 and 585.9 eV, respectively. After Zn doping, the states of Cr $2p_{3/2}$ and $2p_{1/2}$ exhibit a little shift for the $ZnCr_2O_4$ sample, shifting from 576.5 to 575.6 and 585.9 to 585.3 eV, respectively and correlate to Zn^{2+} ions [36]. O-1 s broad and symmetric high-resolution XPS spectrum reveals the existence of different oxygen species, as illustrated in Fig. 3d. One is positioned at 529.5 eV, while the other is located at 531.6 eV. The former is composed of intrinsic O atoms bonded to metals (like Zn and Cr), whereas the latter is connected to O—H. Fig. 3e displays the high-resolution C-1 s XPS spectrum. The three distinct peaks detected at binding energies of 284.5, 286.3, and 288.4 eV are attributed to the chemical bonds C=C, C-C, and C=O, respectively [37].

The as-synthesized ZnO, Cr_2O_3, and $ZnCr_2O_4$ samples were employed as electroactive materials to study their electrochemical performances in a three-electrode setup. CV and GCD tests were performed on the pristine CC to investigate the effect of the substrate on the electrochemical properties. The CV (Fig. S1a) and GCD (Fig. S1b) curves of the pristine CC electrode were performed to find the potential contribution from the CC substrate. It is worth mentioning that the pristine CC electrode has very little discharge time at different current densities from 1 to 20 A/g. The specific capacitance of the pristine CC electrode calculated by the discharge time is also small compared with the $ZnCr_2O_4$, ZnO, and Cr_2O_3 electrodes (Fig. S1c). Therefore, we excluded the capacitance values of the pristine CC electrodes from the $ZnCr_2O_4$, ZnO, and Cr_2O_3 electrodes. The CV measurements were performed on the ZnO, Cr_2O_3, and $ZnCr_2O_4$ samples at 10 mVs^{-1} in a potential window of -0.5 to 0.1 V. It is evident that all these curves demonstrate a nearly rectangular form governed by the electrochemical double layer type charge storage that occur in the aqueous KOH electrolyte (Fig. 4a). The $ZnCr_2O_4$ electrode exhibited an increased integrated area when compared to the ZnO and Cr_2O_3 electrodes, indicating its superior electrochemical performance.

Furthermore, Fig. 4b, c, and d present the characteristic CV curves of ZnO, Cr_2O_3, and $ZnCr_2O_4$ electrodes, respectively, obtained at varying scan rates ranging from 1 to 15 mVs^{-1} in same potential windows. The observed patterns across various scanning rates consistently exhibit a nearly-rectangular shape in all CV curves, suggesting that the charge is stored using an ideal supercapacitive mechanism. The CVs maintain a nearly-rectangular shape even as the scan rate increases, suggesting that the ZnO, Cr_2O_3, and $ZnCr_2O_4$ electrodes exhibit exceptional high ion

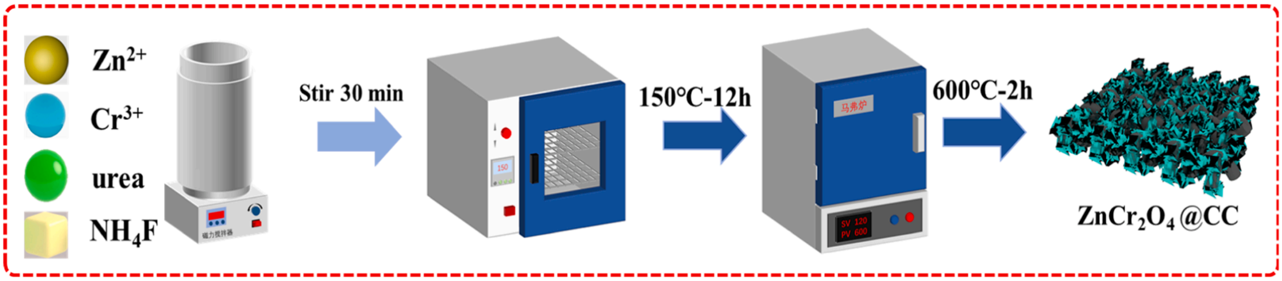

Fig. 1. Schematic depiction of the synthesis process of $ZnCr_2O_4$@CC electrode material.

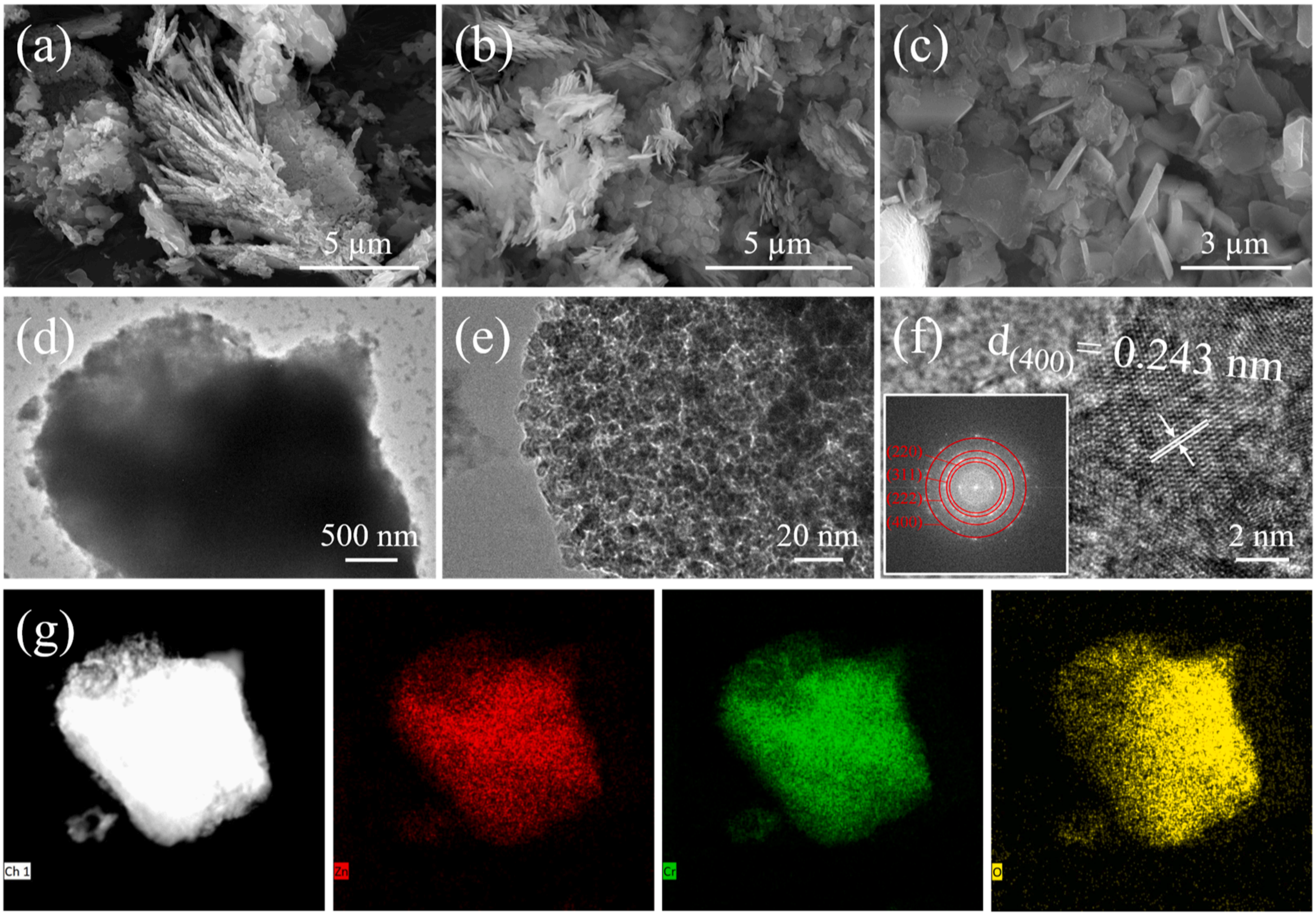

Fig. 2. FESEM images of (a) ZnO; (b) Cr_2O_3; (c) $ZnCr_2O_4$; (d) Low-resolution TEM images of $ZnCr_2O_4$, (e, f) High-resolution TEM images (inset shows the SAED pattern), (g) EDS elemental mapping images for Zn, Cr and O.

transport response. When comparing the ZnO and Cr_2O_3 electrodes, it is observed that the leveled current separation of $ZnCr_2O_4$ is significantly greater. This indicates that the $ZnCr_2O_4$ electrode exhibits superior electrochemical performance. Based on a comprehensive analysis, it is evident that the introduction of Zn-doping has resulted in a pronounced synergistic impact to enhance the performance of $ZnCr_2O_4$ electrode. Additionally, an investigation was conducted to examine the charge storage mechanism in all three electrodes according to following equations [38];

$$i(V) = a.v^b \tag{7}$$

$$\log(i) = b\log(v) + \log(a) \tag{8}$$

Where, *i* is used to represent the peak current density, while *v* is used to denote the scan rate. Additionally, the symbols “a” and “b” are used as arbitrary constants. It is commonly accepted that the diffusion-controlled storage is predominant when the value of *b* is close to 0.5. On the contrary, the capacitive-controlled storage is predominant when the value of *b* is close to 1. According to the relation of log *i* versus log (*v*), ZnO’s anodic and cathodic *b*-values are 0.74 and 0.66, Cr_2O_3’s are 0.91 and 0.88, and $ZnCr_2O_4$’s are 0.74 and 0.66, respectively (Fig. 4e). The following equation was used to calculate quantitative diffusion- and capacitive -controlled contributions of $ZnCr_2O_4$, Cr_2O_3, and ZnO electrode [39];

$$i(V) = k_1 v + k_1 v^{1/2} \tag{9}$$

where, *i* stands for total current, k_1 and k_2 are arbitrary constants, and k_1v and $k_1v^{1/2}$ charge storage via capacitive and diffusion, respectively. The slope and y-intercept of the plots were used to calculate the k_1 and k_2 for $ZnCr_2O_4$ (Fig. S2a), Cr_2O_3 (Fig. S2b), and ZnO (Fig. S2c). Fig. 4f illustrates the charge storage mechanism of the $ZnCr_2O_4$ electrode, indicating that 31.6 % of the charge storage occurs through a capacitive-controlled process at 10 mVs^{-1}. Similarly, the capacitive and diffusion contribution of store charge are 27.6 % for Cr_2O_3 (Fig. S3a) and 11.3 % for ZnO at 10 mVs^{-1} (Fig. S3b). Furthermore, Fig. 4g-i depicts the capacitive and diffusion-controlled mechanisms exhibited by the three electrodes across different scan rates ranging from 1 to 75 mVs^{-1}. The observed trend of increasing capacitive-controlled behavior with higher scan rates suggests that the dominant factor influencing capacitance is the capacitive process, particularly at elevated scan rates for the $ZnCr_2O_4$ electrode.

Fig. 5a depicts the comparative GCD curves obtained for ZnO, Cr_2O_3, and $ZnCr_2O_4$ electrodes at 10 Ag^{-1}. The discharging time of the $ZnCr_2O_4$ electrode is comparatively longer when compared to the Cr_2O_3 and ZnO electrodes. Moreover, the observed IR drop for $ZnCr_2O_4$ electrode (0.02 V) was found to be even smaller than that of the Cr_2O_3 (0.07 V) and ZnO (0.2 V) electrodes, consistent with CV measurements. The remarkably low IR drop and longer discharge time of the $ZnCr_2O_4$ electrode can be ascribed to the extraordinarily high ion conductivity exhibited by the electrode after Zn-doping and electrolyte. Further, the GCD curves of $ZnCr_2O_4$ (Fig. 5b), Cr_2O_3 (Fig. 5c), and ZnO (Fig. 5d) were measured at varied current densities ranging from 1 to 20 Ag^{-1} are presented. The high reversibility and outstanding capacitive property of the $ZnCr_2O_4$ electrode is demonstrated by the GCDs, which are more linear and symmetrical for the $ZnCr_2O_4$ electrode when compared to Cr_2O_3 and

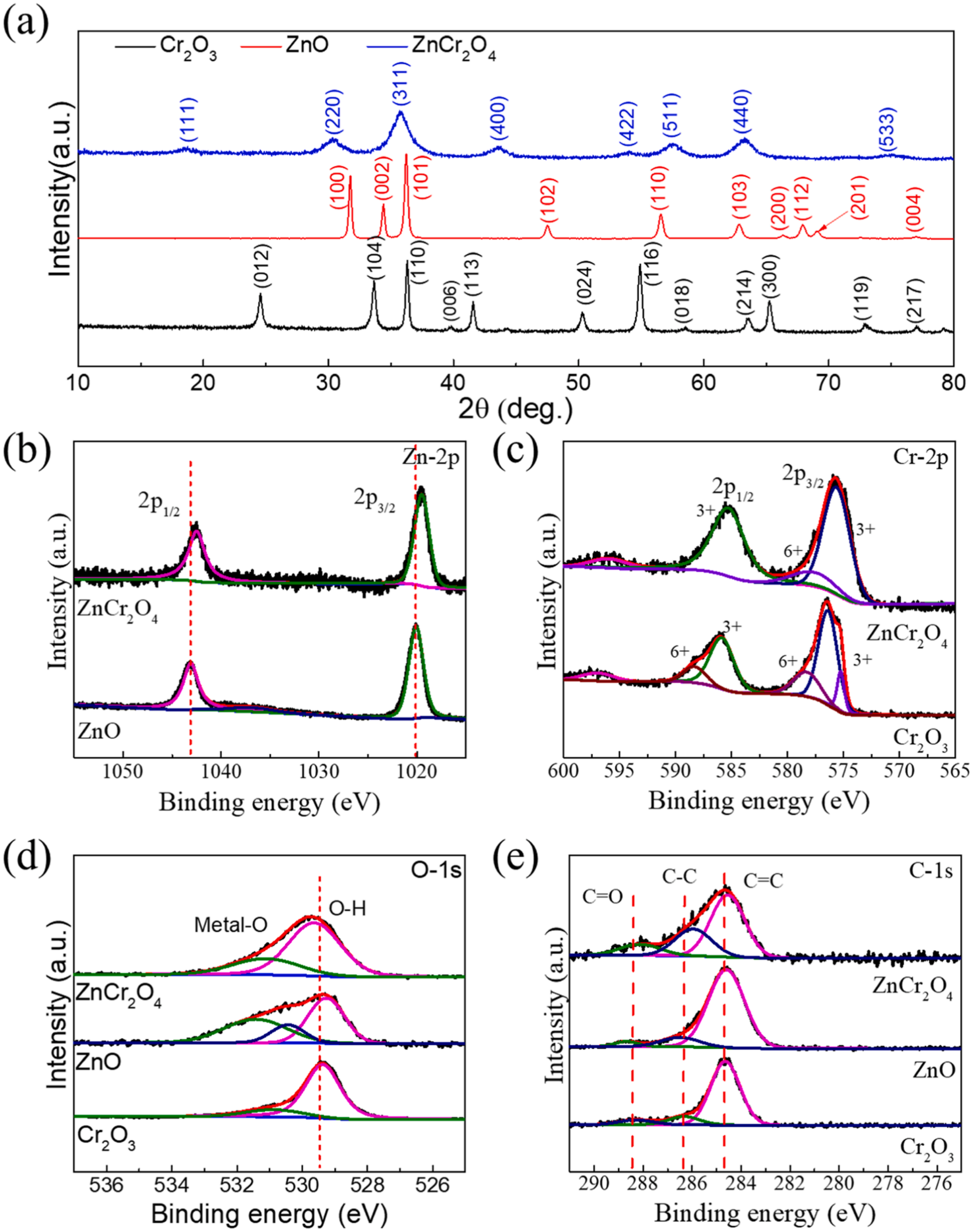

Fig. 3. (a) XRD patterns and high-resolution XPS spectrums of (b) Zn-2p; (c) Cr-2p; (d) O-1 s; (e) C-1 s.

ZnO. The specific capacitance of all three electrodes was determined at various current densities ranging from 1 to 20 Ag^{-1}, and the corresponding results can be observed in Fig. 5e. The $ZnCr_2O_4$ electrode was found to have a maximum specific capacitance of 374 Fg^{-1} at 1 Ag^{-1}. However, the highest specific capacitance at 1 Ag^{-1} was calculated to be 194 Fg^{-1} for the Cr_2O_3 electrode and 60.78 Fg^{-1} for the ZnO electrode. Moreover, the $ZnCr_2O_4$ electrode exhibits a remarkable rate capability of 52.2 % at 20 Ag^{-1}, exceeding both the Cr_2O_3 electrode (33.3 % at 20 Ag^{-1}) and the ZnO electrode (15 % at 20 Ag^{-1}). This characteristic makes it a viable choice for integration into the advancement of next-generation supercapacitors. All three electrode's EIS measurements were taken at open circuit potential to understand the charge storage kinetics. Three Nyquist plots for three electrodes are shown in Fig. 5f. The EIS spectra are composed of a semicircle in the high-frequency region and a linear component in the low-frequency region. In the high-frequency region, the *x*-intercept gives the equivalent series resistance (R_s) value, which includes the intrinsic resistance of the electrode material and solution resistance. The semicircle diameter gives the value of charge transfer resistance (R_{ct}). The slope in the low-frequency region is larger, indicating the small diffusion resistance, enhancing the

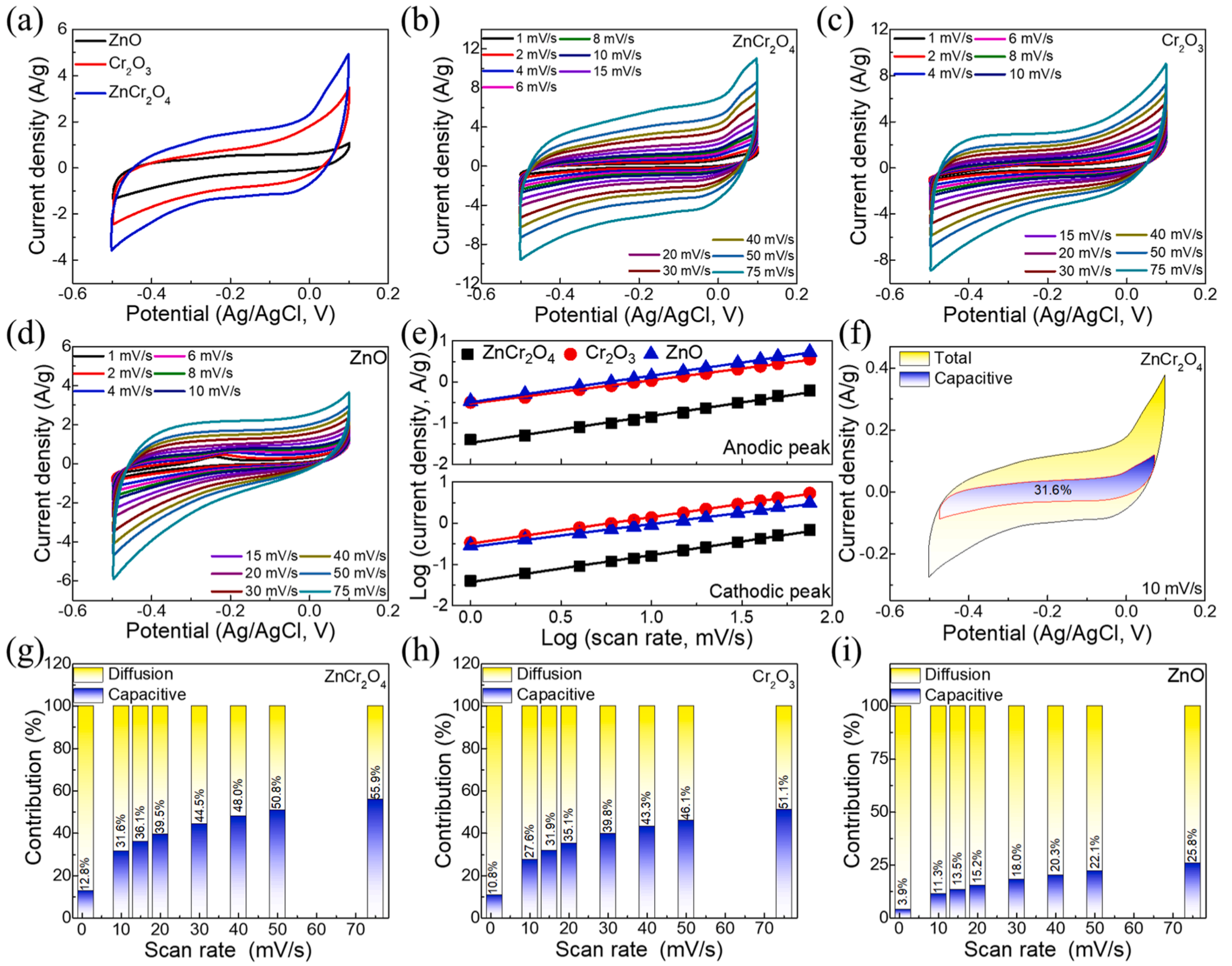

Fig. 4. (a) CV curves of ZnO, Cr_2O_3, and $ZnCr_2O_4$ electrodes at 10 mVs^{-1}; CV curves at various scan rates for (b) $ZnCr_2O_4$; (c) Cr_2O_3; (d) ZnO; (e) Calculations of *b*-values log *i* versus log (*v*); (f) Diffusion and capacitive controlled methods of $ZnCr_2O_4$ electrode; Diffusion- and capacitive-controlled methods contributions at various scan rates for (g) $ZnCr_2O_4$; (h) Cr_2O_3; (i) ZnO.

intercalation effect and improving the power density. The $ZnCr_2O_4$ electrode has the lowest values of R_s = 0.91Ω and R_{ct} = 0.40Ω, compared with Cr_2O_3 (R_s= 1.03Ω and R_{ct} =0.71Ω) and ZnO (R_s = 1.12Ω and R_{ct} = 0.45Ω). Reduced resistance contributes to improved electrochemical performance.

Since the cyclic stability of AHSCs is also of the highest significance for commercial applications, thus, extended cycles are carried out for $ZnCr_2O_4$, Cr_2O_3, and ZnO electrodes at 10 Ag^{-1}. Fig. 5g illustrates the results, indicating that the $ZnCr_2O_4$ electrode exhibits a capacitance retention of 98.6 % after undergoing 10,000 GCD cycles. The Cr_2O_3 and ZnO electrodes retain 97.1 % and 96 % of their initial capacitance, respectively. The repeated GCD cycles demonstrate the remarkable energy-storage capacity of the $ZnCr_2O_4$ electrode.

Ex-situ XPS and XRD techniques were employed to conduct a deep study of the charge storage process of $ZnCr_2O_4$ in an aqueous electrolyte. In the pristine state C-1 s spectra, three peaks, which correspond to C=C, C-C, and C=O, are seen at 284.5, 286.3, and 290.2 eV, respectively (Fig. 6a). Throughout the charging and discharging operation, there was no change in the major peak of C-1 s. Fig. 6b shows that the spectrum of pristine O-1 s has a peak at 530.6 eV that corresponds to O—H. During the charging and discharging, there was no discernible movement in the primary peak of O-1 s. Further, based on the high-resolution spectra of Zn-2p (Fig. 6c) and Cr-2p (Fig. 6d), it can be observed that the primary peaks of Zn-$2p_{3/2}$ at 1020.2 eV, Cr-$2p_{3/2}$ at 576.6 eV, and Cr-$2p_{1/2}$ at 586.3 eV experience a slight shift towards lower binding energy during the discharging process. However, these peaks return to their original positions after the charging process, indicating the electrode material's high stability without any major phase change in the structure.

XRD analysis was conducted to elucidate the structural changes in the $ZnCr_2O_4$ electrode, as depicted in Fig. 7. The associated specific characteristic peaks exhibit minimal changes throughout the charge and discharge cycles, suggesting a high degree of reversibility in the K^+ intercalation/deintercalation process. Following the initial process of charging and discharging in an aqueous electrolyte, it has been observed that the material's crystallinity is effectively maintained. No observable displacement of the XRD peaks was detected during the charge and discharge procedure. This observation implies no noticeable structural change in the composition or lattice parameters. Hence, the XRD investigation reveals that the storage of charge is attributed to capacitive processes, supporting the findings of the XPS analysis. Due to the reversible nature of the K^+ intercalation/deintercalation process, the $ZnCr_2O_4$ electrode exhibits good cyclability.

Furthermore, Table 1 summarizes the electrochemical performance of ZnCr2O4 compared to the electrochemical performance of other transition metal oxide-based electrodes for SCs. According to the comparison findings, the electrochemical performance of the ZnCr2O4

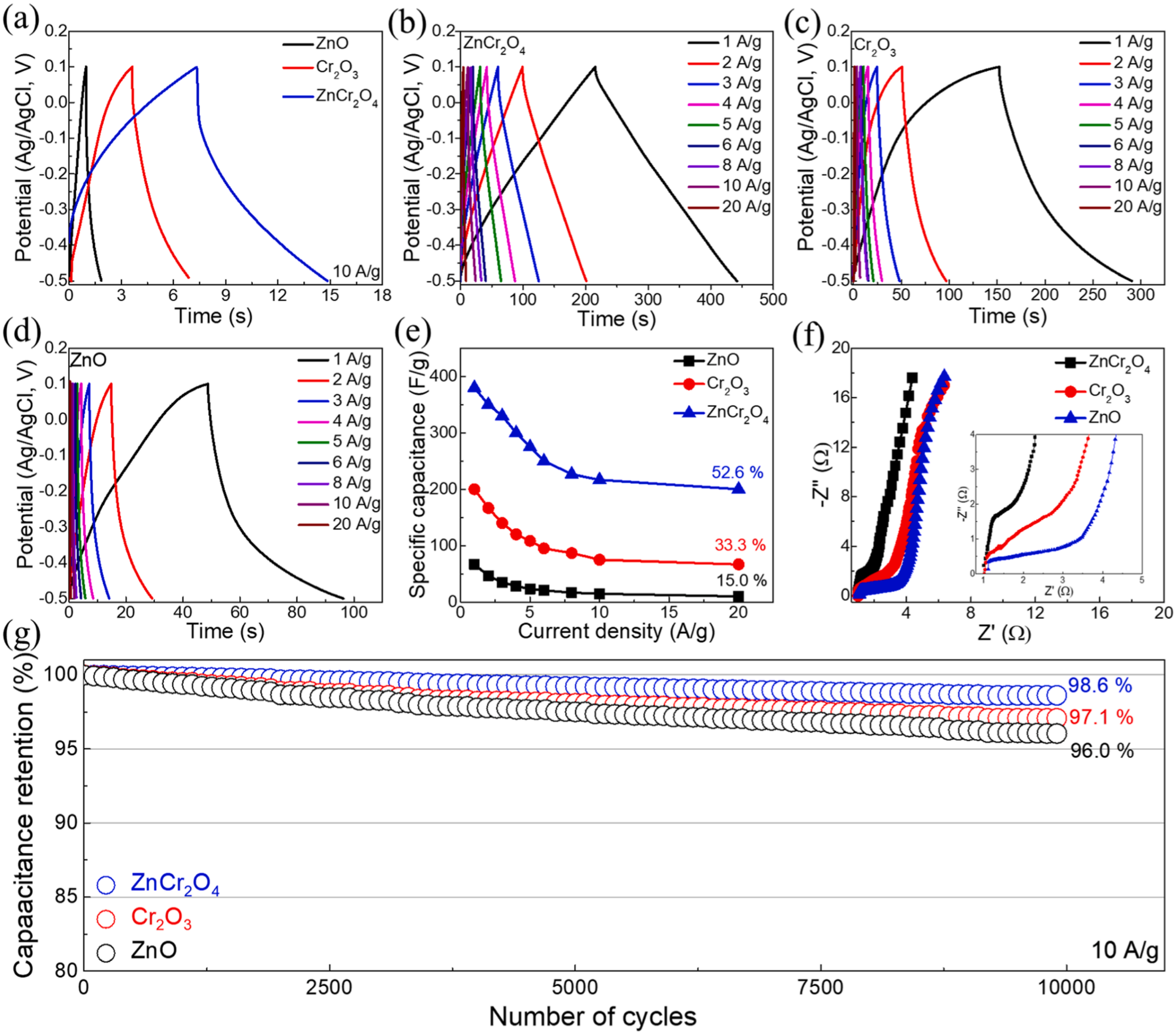

Fig. 5. (a) GCD curves of ZnO, Cr_2O_3, and $ZnCr_2O_4$ electrodes at 10 Ag^{-1}; GCD curves at various current densities for (b) $ZnCr_2O_4$; (c) Cr_2O_3; (d) ZnO; (e) Specific capacitance as function of current density for ZnO, Cr_2O_3, and $ZnCr_2O_4$ electrodes; (f) Nyquist plots (inset shows the enlarged view at high-frequency region); (g) Cycling stability test for three electrodes.

electrode is better than that of other comparable materials that have been examined in the past.

To investigate the feasibility of $ZnCr_2O_4$ as a positive electrode (cathode), an AHSC device ($ZnCr_2O_4$@CC//AC-AHSC) was developed using activated carbon (AC) as a negative electrode (anode) and 1 M KOH as an aqueous electrolyte. Fig. 8a provides an illustration of both the assembly and the working principle of the AHSC. The results of a CV measurement were conducted at 10 mVs^{-1} on $ZnCr_2O_4$ and AC electrodes within their designated potential ranges (Fig. 8b). The CV curves provide evidence of the properties exhibited by a pseudocapacitor in the $ZnCr_2O_4$ electrode. In contrast, the AC electrode displayed the features of an electrical double layer. Based on the charge balance equation, the masses of the anode and cathode were adjusted for the fabrication of the AHSC [49].

$$\frac{m^{+}}{m^{-}} = \frac{(C^{-} \times \ \Delta V^{-})}{(C^{-} \times \ \Delta V^{+})} \tag{10}$$

Where, C^+ and C^- stand for the specific capacitance of the cathode and anode, respectively; m^+ and m^- stand for the masses of the cathode and anode; and V^+ and V^- stand for the potential difference between the cathode and anode. Fig. 8c displays the CV curves of $ZnCr_2O_4$@CC//AC-AHSC at different scan rates, ranging from 1 to 75 mVs^{-1}, within a potential range of 0 to 1.6 V. Even when the scan rates were increased, the CV curves maintained their shapes with minimal alterations, and the area under the CVs exhibited a gradual increase with scan rates. The results suggest that $ZnCr_2O_4$@CC//AC-AHSC exhibits a notable hybrid-pseudocapacitive response and satisfactory charge/discharge capacity, demonstrating outstanding electrochemical performance [50]. As shown in Fig. 8d, the GCD curves were carried out in a potential window of 0 to 1.6 V at current densities ranging from 1 to 20 Ag^{-1}. The GCD curves seen in $ZnCr_2O_4$@CC//AC-AHSC are indicative of the pseudocapacitive charge storage. Eq. (2) is used to determine the maximum specific capacitance (C_d) for the $ZnCr_2O_4$@CC//AC-AHSC device based on the total mass of active material on both the cathode and anode and the discharging time. According to Fig. 8e, the maximum specific capacitance value achieved 73.75 Fg^{-1} at 1 Ag^{-1}. To get insight into the

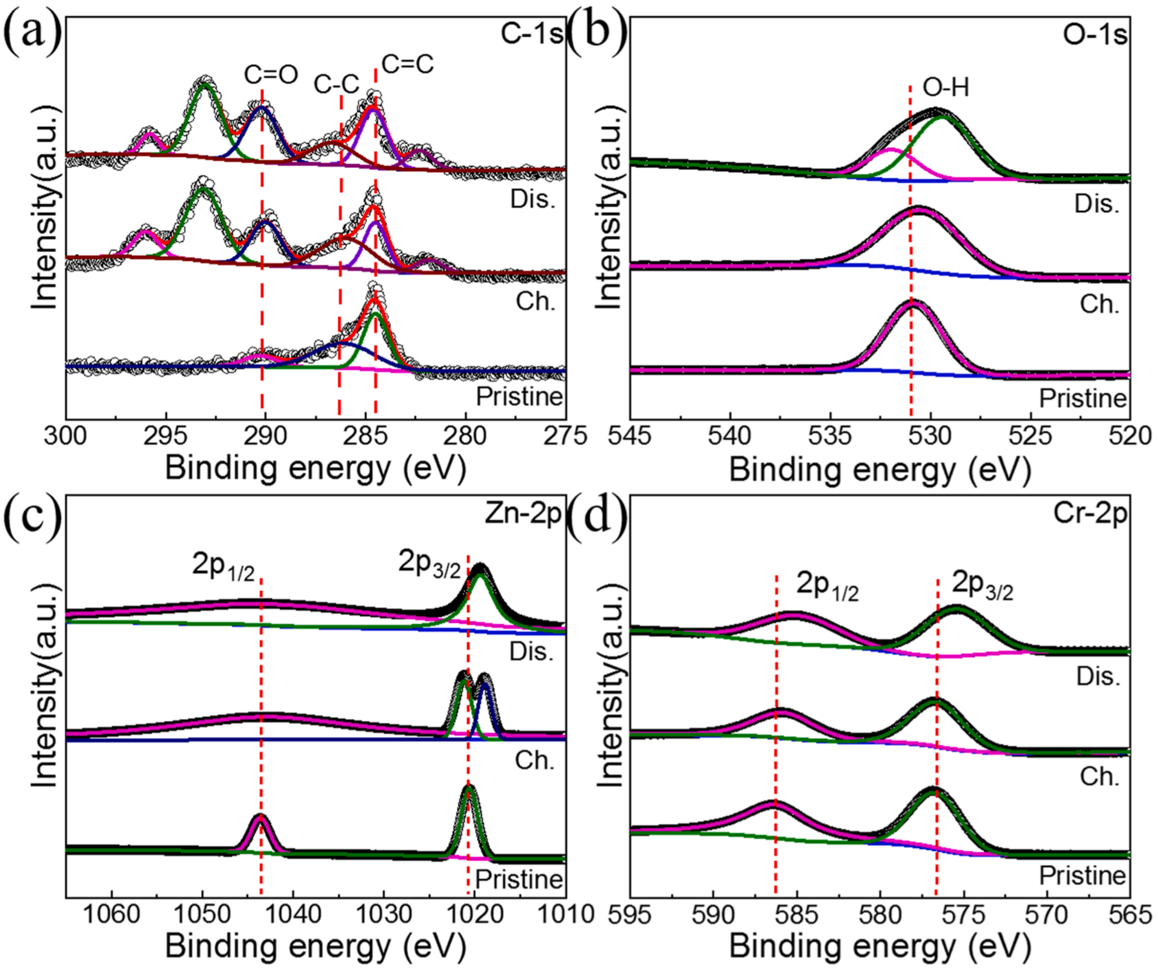

Fig. 6. Ex-situ high-resolution XPS spectrum for pristine and after charge and discharge process of (a) C-1 s; (b) O-1 s; (c) Zn-2p; (d) Cr-2p.

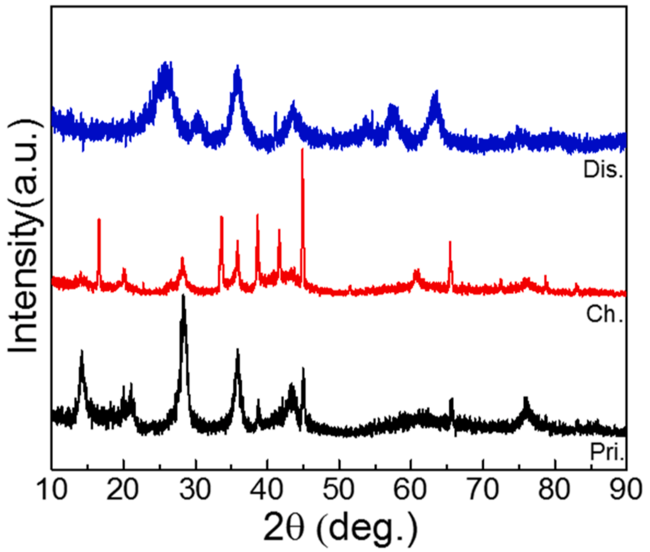

Fig. 7. Ex-situ XRD patterns of $ZnCr_2O_4$ electrode pristine, charge, and discharge states.

practical performance of the $ZnCr_2O_4$@CC//AC-AHSC device, E and P were computed using Eqs. (3) and (4), respectively. Fig. 8f displays the Ragone plot, which illustrates the E versus P characteristics of the $ZnCr_2O_4$@CC//AC-AHSC device. The $ZnCr_2O_4$@CC//AC-AHSC device exhibits the highest energy density of 26.2 Whkg^{-1} at a power density of 800.6 Wkg^{-1}. Furthermore, the current $ZnCr_2O_4$@CC//AC-AHSC device is superior to several other previously explored asymmetric SC devices, including $ZnCo_2O_4$@$MnCo_2O_4$//AC (19.5 Whkg^{-1} at 750 Wkg^{-1}) [51], Co_3O_4//AC (22.49 Whkg^{-1} at 800 Wkg^{-1}) [52], $CoSe_2$@CNT/C-C//AC@CC (18.9 Whkg^{-1} at 387 Wkg^{-1}) [53], $ZnCo_2O_4$—CNT//AC (24.5 Whkg^{-1} at 750 Wkg^{-1}) [54] and Co_3O_4 nanoparticles//rGO (13.51 Whkg^{-1} at 844 Wkg^{-1}) [55].

Additionally, Fig. 8g displays the cycling stability of the $ZnCr_2O_4$@CC//AC-AHSC device, which demonstrates a retention rate of 96.43 % after 10,000 GCD cycles, indicating an exceptional cycling performance. According to the findings of the three- and two-electrode systems, the $ZnCr_2O_4$ electrode has an outstanding electrochemical performance. This exceptional performance can be seen in specific capacitance, cyclic stability, and energy/power densities. It is concluded that the synergic effects of composition between Zn and Cr_2O_3 in the $ZnCr_2O_4$ electrode play an important role in these amazing characteristics.

4. Conclusion

A facile hydrothermal method was used to fabricate the Zn-doped Cr_2O_3 supported on the CC electrode for AHSCs. According to the experimental results, the $ZnCr_2O_4$ electrode demonstrates a fast charge transfer. As a consequence, the $ZnCr_2O_4$ electrode delivered a remarkable charge storage performance with dominant charge storage by capacitive-type (68.4 % at 10 mVs^{-1}) and shows a maximum capacitance of 374 Fg^{-1} at 1 Ag^{-1} and outperforms its counterparts (194 Fg^{-1}

Table 1
A comparison of the current study with previously reported transition metal oxide-based electrodes.

Sr. No.	Electrodes	Electrolyte	Specific Capacitance (Fg^{-1})	Current Density (Ag^{-1})	No. of Cycles	Capacitance retention (%)	Ref.
1	$ZnCr_2O_4$	KOH	374	1	10,000	98.6	This work
2	rGO/ZnO	KOH	312	1	1000	95	[40]
3	$MnO_2/MnCo_2O_4$	KOH	497	0.5	5000	60	[41]
4	Cr_2O_3/Ni foam	KOH	130	1	3000	89.8	[42]
5	Cr_2O_3/C	KOH	291	0.25	3000	95.5	[43]
6	Cr_2O_3–NiO	KOH	333.4	1	2000	87.7	[44]
7	Al doped $NiFe_2O_4$	Na_2SO_4	250.9	0.5	1000	96	[45]
8	Cr_2O_3	Na_2SO_4	340	0.5	3000	85	[46]
9	ZnO/rGO/ZnO	Na_2SO_4	275	0.5	1000	98	[47]
10	$CoFe_2O_4$/rGO	KOH	194	1	2500	71.9	[48]

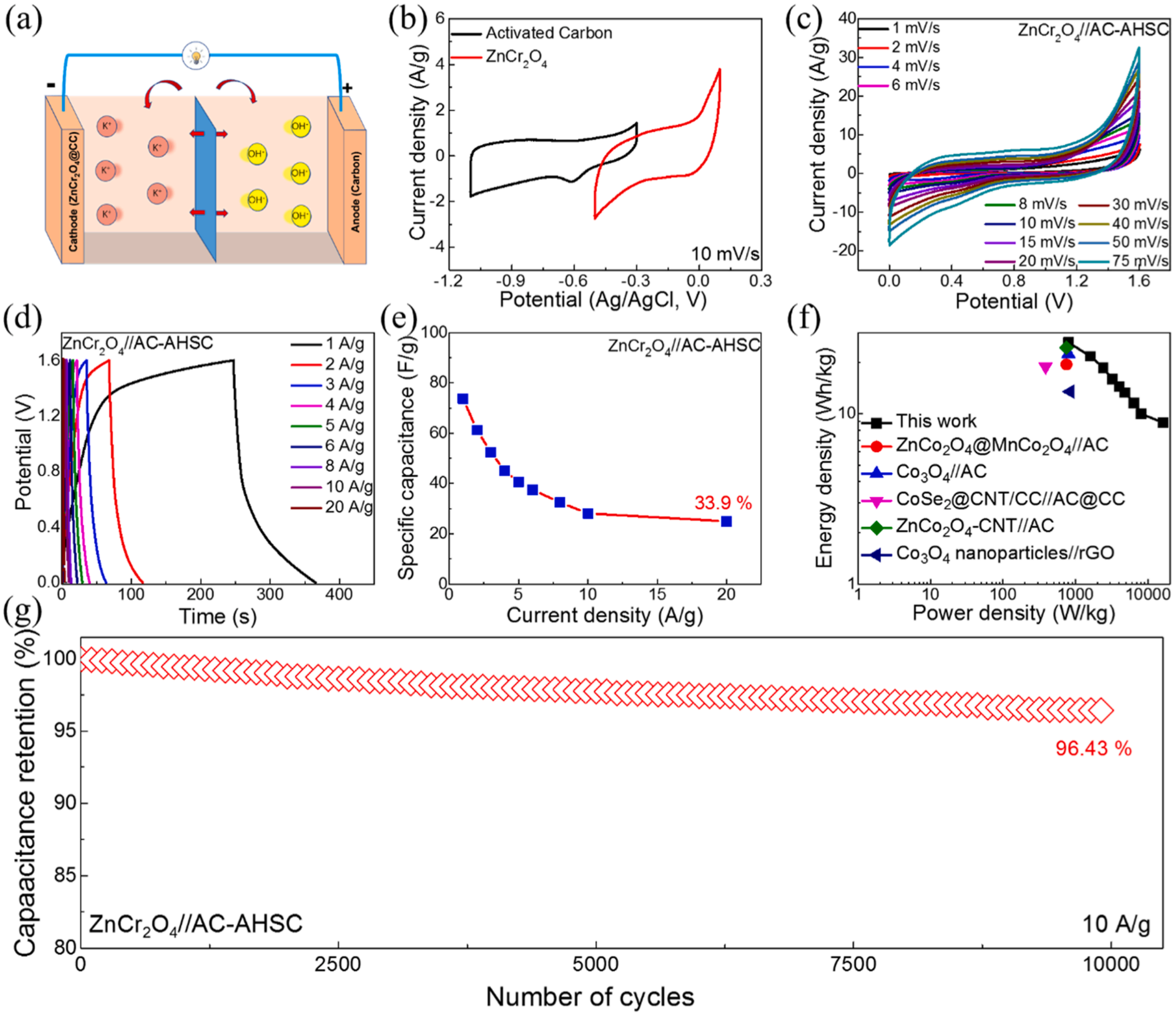

Fig. 8. Electrochemical characterization of $ZnCr_2O_4$@CC//AC-AHSC device in two-electrode configuration: (a) Schematic illustration for the fabrication and working principle of AHSC device; (b) CV curves of cathode and anode at 10 mVs^{-1}; (c) CV curves of AHSC device at different scan rates; (d) GCDs at different current densities; (e) Specific capacitance versus current density; (f) Ragone plot compared with previous literature; (g) Cyclic stability test upto 10,000 cycles.

for Cr_2O_3 and 60.78 Fg^{-1} for ZnO). The $ZnCr_2O_4$ electrode also exhibits 98.1 % of its initial capacitance after 10,000 cycles, demonstrating its potential for application in the emerging domain of sustainable energy storage devices. In addition, the $ZnCr_2O_4$@CC//AC-AHSC device is constructed using $ZnCr_2O_4$ as a cathode and AC as an anode. The $ZnCr_2O_4$@CC//AC-AHSC device demonstrates an excellent capacitance retention of 96.43 % after 10,000 cycles. Furthermore, the $ZnCr_2O_4$@CC//AC-AHSC delivers an excellent energy density of 26.2 $Whkg^{-1}$ at a power density of 800.6 Wk−1 g. Because of the synergistic properties of Zn and Cr_2O_3, the $ZnCr_2O_4$ electrode provides exceptional good electrochemical performance. This study presents a novel approach for fabricating advanced electrode materials for AHSCs, exhibiting remarkable electrochemical characteristics.

CRediT authorship contribution statement

Tianyang Fei: Conceptualization, Data curation, Formal analysis, Writing – original draft, Writing – review & editing. **Tauqeer Ahmad:** Data curation, Formal analysis, Investigation, Writing – original draft. **Muhammad Usman:** Data curation, Software, Writing – original draft, Writing – review & editing. **Awais Ahmad:** Conceptualization, Data curation, Investigation, Visualization, Writing – original draft, Writing – review & editing. **Adil Saleem:** Conceptualization, Software, Visualization, Writing – original draft, Writing – review & editing. **Muhammad Bilal Hanif:** Data curation, Formal analysis, Methodology, Writing – review & editing. **Abdulnasser M. Karami:** Formal analysis, Project administration, Software, Validation, Writing – original draft. **Muhammad Sufyan Javed:** Conceptualization, Data curation, Supervision. **Bhargav Akkinepally:** Conceptualization, Formal analysis, Methodology, Writing – original draft, Writing – review & editing. **Changlei Xia:** Conceptualization, Funding acquisition, Project administration, Supervision, Visualization, Writing – review & editing.

Declaration of Competing Interest

Data availability

Data will be made available on request.

Acknowledgment

The authors acknowledge the scientific and technical input and support from the School of Physical Science and Technology, Lanzhou University, China. This work was financially supported by the scientific research start-up grant for Youth Researchers at Lanzhou University. This work was funded by the Researchers Supporting Project Number (RSPD2023R764), King Saud University, Riyadh, Saudi Arabia.

Supplementary materials

Supplementary material associated with this article can be found, in the online version, at doi:10.1016/j.electacta.2023.143673.

References

[1] M.S. Javed, A. Mateen, I. Hussain, A. Ahmad, M. Mubashir, S. Khan, M.A. Assiri, S. M. Eldin, S.S.A. Shah, W. Han, Recent progress in the design of advanced MXene/metal oxides-hybrid materials for energy storage devices, Energy Storage Mater. 53 (2022) 827–872.

[2] B. Liu, X. Wang, Y. Chen, H. Xie, X. Zhao, A.B. Nassr, Y. Li, Honeycomb carbon obtained from coal liquefaction residual asphaltene for high-performance supercapacitors in ionic and organic liquid-based electrolytes, J. Energy Storage 68 (2023), 107826, https://doi.org/10.1016/j.est.2023.107826.

[3] X. Feng, L. Sun, W. Wang, Y. Zhao, J.W. Shi, Construction of CdS@ZnO core–shell nanorod arrays by atomic layer deposition for efficient photoelectrochemical H2 evolution, Sep. Purif. Technol. 324 (2023), 124520, https://doi.org/10.1016/j.seppur.2023.124520.

[4] D. Wang, X.X. Wang, M.L. Jin, P. He, S. Zhang, Molecular level manipulation of charge density for solid-liquid TENG system by proton irradiation, Nano Energy 103 (2022), 107819, https://doi.org/10.1016/j.nanoen.2022.107819.

[5] S. Li, J. Chen, X. He, Y. Zheng, C. Yu, H. Lu, Comparative study of the micro-mechanism of charge redistribution at metal-semiconductor and semimetal-semiconductor interfaces: pt(Ni)-MoS_2 and Bi-MoS_2(WSe_2) as the prototype, Appl. Surf. Sci. 623 (2023), 157036, https://doi.org/10.1016/j.apsusc.2023.157036.

[6] C. Lu, R. Ren, Z. Zhu, G. Pan, G. Wang, C. Xu, J. Qiao, W. Sun, Q. Huang, H. Liang, Z. Wang, K. Sun, $BaCo_{0.4}Fe_{0.4}Nb_{0.1}Sc_{0.1}O_3$-δ perovskite oxide with super hydration capacity for a high-activity proton ceramic electrolytic cell oxygen electrode, Chem. Eng. J. 472 (2023), 144878, https://doi.org/10.1016/j.cej.2023.144878.

[7] X. Cai, X. Li, J. You, F. Yang, Z. Shadike, S. Qin, L. Luo, Y. Guo, X. Yan, S. Shen, G. Wei, Z.J. Xu, J. Zhang, Lithium-mediated ammonia electrosynthesis with ether-based electrolytes, J. Am. Chem. Soc. 145 (47) (2023) 25716–25725, https://doi.org/10.1021/jacs.3c08965.

[8] H. Yu, D. Chen, Q. Li, C. Yan, Z. Jiang, L. Zhou, W. Wei, J. Ma, X. Ji, Y. Chen, L. Chen, *In situ* construction of anode–molecule interface via lone-pair electrons in trace organic molecules additives to achieve stable zinc metal anodes, Adv. Energy Mater. 13 (22) (2023), 2300550, https://doi.org/10.1002/aenm.202300550.

[9] M.S. Saleem, M.B. Hanif, M. Gregor, M. Motola, A.F. Khan, Nanostructured multi-layer MgF_2/ITO coatings prepared via e-beam evaporation for efficient electromagnetic interference shielding performance, Appl. Surf. Sci. 596 (2022) 153584.

[10] J. Zhao, M. Zhou, J. Chen, L. Wang, Q. Zhang, S. Zhong, H. Xie, Y. Li, Two birds one stone: graphene assisted reaction kinetics and ionic conductivity in phthalocyanine-based covalent organic framework anodes for lithium-ion batteries, Small 19 (44) (2023), 2303353, https://doi.org/10.1002/smll.202303353.

[11] L. Wang, Y. Jiang, S.Y. Li, X.H. Chen, F.S. Xi, X.H. Wan, W.H. Ma, R. Deng, Scalable synthesis of N-doped Si/G@voids@C with porous structures for high-performance anode of lithium-ion batteries, Rare Met. 42 (12) (2023) 4091–4102, https://doi.org/10.1007/s12598-023-02472-0.

[12] X. Li, S. Aftab, A. Abbas, S. Hussain, M. Aslam, F. Kabir, H.S.M. Abd-Rabboh, H. H. Hegazy, F. Xu, M.Z. Ansari, Advances in mixed 2D and 3D perovskite heterostructure solar cells: a comprehensive review, Nano Energy 118 (2023), 108979, https://doi.org/10.1016/j.nanoen.2023.108979.

[13] A.A. Safri, J. Ur Rehman, S. Shabbir, W. Hussain, Bacterial disinfection using polymer based hybrids, Key Eng. Mater. 778 (2018) 331–335.

[14] X. Zhang, Y. Tang, F. Zhang, C.S. Lee, A novel aluminum–graphite dual-ion battery, Adv. Energy Mater. 6 (11) (2016), 1502588, https://doi.org/10.1002/aenm.201502588.

[15] S. Mu, Q. Liu, P. Kidkhunthod, X. Zhou, W. Wang, Y. Tang, Molecular grafting towards high-fraction active nanodots implanted in N-doped carbon for sodium dual-ion batteries, Natl. Sci. Rev. 8 (7) (2020), https://doi.org/10.1093/nsr/nwaa178.

[16] B. Ji, F. Zhang, X. Song, Y. Tang, A novel potassium-ion-based dual-ion battery, Adv. Mater. 29 (19) (2017), 1700519, https://doi.org/10.1002/adma.201700519.

[17] X. Tong, F. Zhang, B. Ji, M. Sheng, Y. Tang, Carbon-coated porous aluminum foil anode for high-rate, long-term cycling stability, and high energy density dual-ion batteries, Adv. Mater. 28 (45) (2016) 9979–9985, https://doi.org/10.1002/adma.201603735.

[18] M. Wang, C. Jiang, S. Zhang, X. Song, Y. Tang, H.M. Cheng, Reversible calcium alloying enables a practical room-temperature rechargeable calcium-ion battery with a high discharge voltage, Nat. Chem. 10 (6) (2018) 667–672, https://doi.org/10.1038/s41557-018-0045-4.

[19] H. Yu, D. Chen, X. Ni, P. Qing, C. Yan, W. Wei, J. Ma, X. Ji, Y. Chen, L. Chen, Reversible adsorption with oriented arrangement of a zwitterionic additive stabilizes electrodes for ultralong-life Zn-ion batteries, Energy Environ. Sci. 16 (6) (2023) 2684–2695, https://doi.org/10.1039/D3EE00982C.

[20] A. Mateen, M.S. Javed, X. Zhang, I. Hussain, T. Najam, A. Ahmad, A.A. Alothman, M. Ouladsmane, S.M. Eldin, W. Han, K.Q. Peng, Two birds with one stone: cobalt/silicon species encapsulated in MOF-derived nitrogen-doped carbon as an integrated electrode for next-generation symmetric pseudocapacitors with energy density over 100W h kg−1, J. Mater. Chem. A 11 (22) (2023) 11804–11818.

[21] S. Yetiman, H. Peçenek, F.K. Dokan, M.S. Onses, E. Yılmaz, E. Sahmetlioglu, Microwave-assisted fabrication of high-performance supercapacitors based on electrodes composed of cobalt oxide decorated with reduced graphene oxide and carbon dots, J. Energy Storage 49 (2022), 104103.

[22] M.S. Javed, X. Zhang, S. Ali, A. Mateen, M. Idrees, M. Sajjad, S. Batool, A. Ahmad, M. Imran, T. Najam, W. Han, Heterostructured bimetallic–sulfide@layered Ti3C2Tx–MXene as a synergistic electrode to realize high-energy-density aqueous hybrid-supercapacitor, Nano Energy 101 (2022), 107624.

[23] P. Xu, Q. Yuan, W. Ji, R. Yu, F. Wang, N. Huo, Study on the annealing phase transformation mechanism and electrochemical properties of carbon submicron fibers loaded with cobalt, Mater. Exp. 12 (12) (2022) 1493–1501.

[24] X. Xu, J. Wu, N. Yang, H. Na, L. Li, J.J.M.L. Gao, Cr2O3: a novel supercapacitor electrode material with high capacitive performance, Mater. Lett. 142 (2015) 172–175.

[25] B. Chen, Y. Wang, C. Li, L. Fu, X. Liu, Y. Zhu, L. Zhang, Y.J.R.a. Wu, A Cr_2O_3/MWCNTs composite as a superior electrode material for supercapacitor, RSC Adv. 7 (40) (2017) 25019–25024.

[26] P. Kharade, S. Chavan, S. Mane, P. Joshi, D.J.J.o.t.C.A.M.S. Salunkhe, Synthesis and characterization of galvanostatically deposited Cr_2O_3, Mn_3O_4, Cr_2O_3/Mn_3O_4 layered composite thin film for supercapacitor application, J. Chinese Adv. Mater. Soc. 4 (1) (2016) 1–12.

[27] T. Li, Z. Liu, L. Zhu, F. Dai, L. Hu, L. Zhang, Z. Wen, Y.J.J.o.M.S. Wu, Cr_2O_3 nanoparticles: a fascinating electrode material combining both surface-controlled and diffusion-limited redox reactions for aqueous supercapacitors, J. Mater. Sci. 53 (24) (2018) 16458–16465.

[28] I. Shafi, E. Liang, B. Li, Ultrafine chromium oxide (Cr_2O_3) nanoparticles as a pseudocapacitive electrode material for supercapacitors, J. Alloys Compd. 851 (2021), 156046.

[29] X. Xu, J. Gao, W. Hong, Ni-based chromite spinel for high-performance supercapacitors, RSC Adv. 6 (35) (2016) 29646–29653.

[30] X. Zhang, M. Suneetha, M. Usman, T. Ahmad, S. Ali, M.S.S. Khan, A.M. Hassan, S. E. Elkhatib, M. Ouladsmane, Chromium induced nickel oxides leads to extraordinary enhancement in the performance of aqueous hybrid supercapacitors, Electrochim. Acta 467 (2023), 143093.

[31] S. Ghosh, S. Barg, S.M. Jeong, K. Ostrikov, Heteroatom-doped and oxygen-functionalized nanocarbons for high-performance supercapacitors, 10(32) (2020) 2001239.

[32] S.J. Uke, S.P. Mardikar, D.R. Bambole, Y. Kumar, G.N. Chaudhari, Sol-gel citrate synthesized Zn doped $MgFe_2O_4$ nanocrystals: a promising supercapacitor electrode material, Mater. Sci. Energy Technol. 3 (2020) 446–455.

[33] A. Joseph, S. Ramachandran, T. Thomas, Ball milling nanoarchitectonics of nitrogen-doped Cr_2O_3 on thermally exfoliated. a. morphous nanosheets for a high-performance supercapacitor, ChemistrySelect 8 (25) (2023), e202300808, https://doi.org/10.1002/slct.202300808.

[34] S. Ma, Y. Xu, X. Cheng, X. Zhang, S. Gao, H. Zhao, L. Huo, Green and facile synthesis of porous hierarchical Cr_2O_3/N-doped carbon composite with high Li-ion battery anodic performance, Int. J. Electrochem. Sci. 13 (2018) 6048–6058.

[35] X. Wang, P. Xu, P. Zhang, S. Ma, Preparation of electrode materials based on carbon cloth via hydrothermal method and their application in supercapacitors, Materials (Basel) 14 (23) (2021) 7148.

[36] S. Ren, G. Sun, J. Zhao, J. Dong, Y. Wei, Z. Ma, X. Zhao, W.J.A.P.L. Chen, Electric field-induced magnetic switching in Mn: ZnO film, Appl. Phys. Lett. 104 (23) (2014).

[37] Y. Zheng, Y. Liu, X. Guo, Z. Chen, W. Zhang, Y. Wang, X. Tang, Y. Zhang, Y. Zhao, Sulfur-doped g-C_3N_4/rGO porous nanosheets for highly efficient photocatalytic degradation of refractory contaminants, J. Mater. Sci. Mater. Med. 41 (2020) 117–126, https://doi.org/10.1016/j.jmst.2019.09.018.

[38] T. Xu, Z. Li, D. Wang, M. Zhang, L. Ai, Z. Chen, J. Zhang, X. Zhang, L.J.A.F.M. Shen, A fast proton-induced pseudocapacitive supercapacitor with high energy and power density, Adv. Funct. Mater. 32 (5) (2022), 2107720.

[39] D. Chao, C. Zhu, M. Song, P. Liang, X. Zhang, N.H. Tiep, H. Zhao, J. Wang, R. Wang, H.J.A.M. Zhang, A high-rate and stable quasi-solid-state zinc-ion battery with novel 2D layered zinc orthovanadate array, Adv. Mater. 30 (32) (2018), 1803181.

[40] J. Jayachandiran, J. Yesuraj, M. Arivanandhan, A. Raja, S.A. Suthanthiraraj, R. Jayavel, D.J.J.o.I. Nedumaran, O. polymers, materials, synthesis and electrochemical studies of rGO/ZnO nanocomposite for supercapacitor application, J. Inorg. Organomet. Polym. Mater. 28 (2018) 2046–2055.

[41] Y. Zhang, H. Xuan, Y. Xu, B. Guo, H. Li, L. Kang, P. Han, D. Wang, Y.J.E.A. Du, One-step large scale combustion synthesis mesoporous MnO_2/$MnCo_2O_4$ composite as electrode material for high-performance supercapacitors, Electrochim. Acta 206 (2016) 278–290.

[42] X. Xu, J. Wu, N. Yang, H. Na, L. Li, J. Gao, Cr_2O_3: a novel supercapacitor electrode material with high capacitive performance, Mater. Lett. 142 (2015) 172–175.

[43] S. Ullah, I.A. Khan, M. Choucair, A. Badshah, I. Khan, M.A.J.E.A. Nadeem, A novel Cr_2O_3-carbon composite as a high performance pseudo-capacitor electrode material, Electrochim. Acta 171 (2015) 142–149.

[44] G. Maheshwaran, C. Selvi, R. Kaliammal, M.Ramesh Prabhu, M.Krishna Kumar, S. Sudhahar, Exploration of Cr_2O_3-NiO nanocomposite as a superior electrode material for supercapacitor applications, Mater. Lett. 300 (2021), 130191.

[45] P. Ramadevi, A. Sangeetha, F. Kousi, R.J.M.T.P. Shanmugavadivu, Structural and electrochemical investigation on pure and aluminium doped nickel ferrite nanoparticles for supercapacitor application, Mater. Today: Proc. 33 (2020) 2116–2121.

[46] I. Shafi, E. Liang, B.J.J.o.A. Li, Compounds, ultrafine chromium oxide (Cr_2O_3) nanoparticles as a pseudocapacitive electrode material for supercapacitors, J. Alloys Compd. 851 (2021), 156046.

[47] Z. Li, P. Liu, G. Yun, K. Shi, X. Lv, K. Li, J. Xing, B.J.E. Yang, 3D (Three-dimensional) sandwich-structured of ZnO (zinc oxide)/rGO (reduced graphene oxide)/ZnO for high performance supercapacitors, Energy 69 (2014) 266–271.

[48] K.V. Sankar, R.K. Selvan, D.J.R.A. Meyrick, Electrochemical performances of $CoFe_2O_4$ nanoparticles and a rGO based asymmetric supercapacitor, RSC Adv. 5 (121) (2015) 99959–99967.

[49] M. Karuppaiah, R. Akilan, P. Sakthivel, S. Asaithambi, R. Shankar, R. Yuvakkumar, Y. Hayakawa, G.J.J.o.E.S. Ravi, Synthesis of self-assembled micro/nano structured manganese carbonate for high performance, long lifespan asymmetric supercapacitors and investigation of atomic-level intercalation properties of OH− ions via first principle calculation, J. Energy Storage 27 (2020), 101138.

[50] C. Shi, Q. Yang, S. Chen, Y. Xue, Y. Hao, Y.J.A.A.E.M. Yan, Granular nanosheets made of interconnected $NiTe_2$-$CoTe_2$ nanoparticles on carbon fibers for high-performance hybrid supercapacitors, ACS Appl. Energy Mater. 5 (3) (2022) 2817–2825.

[51] L. Wang, Y. Guan, X. Zhao, J. Mu, H. Che, H. Li, Z. Guo, $ZnCo_2O_4$@ $MnCo_2O_4$ heterojunction structured nanosheets for high-performance supercapacitor, J. Mater. Sci. Mater. Electron. 29 (7) (2018) 5782–5790.

[52] J. Zhu, B. Huang, C. Zhao, H. Xu, S. Wang, Y. Chen, L. Xie, L. Chen, Benzoic acid-assisted substrate-free synthesis of ultrathin nanosheets assembled two-dimensional porous Co3O4 thin sheets with 3D hierarchical micro-/nano-structures and enhanced performance as battery-type materials for supercapacitors, Electrochim. Acta 313 (2019) 194–204.

[53] M. Sajjad, M. Amin, M.S. Javed, M. Imran, W. Hu, Z. Mao, W. Lu, Recent trends in transition metal diselenides (XSe2: X= Ni, Mn, Co) and their composites for high energy faradic supercapacitors, J. Energy Storage 43 (2021), 103176.

[54] L. Wu, L. Sun, X. Li, Q. Zhang, H. Si, Y. Zhang, K. Wang, Y. Zhang, Mesoporous $ZnCo_2O_4$-CNT microflowers as bifunctional material for supercapacitive and lithium energy storage, Appl. Surf. Sci. 506 (2020), 144964.

[55] H. Bigdeli, M. Moradi, S. Hajati, M.A. Kiani, J. Toth, Cobalt terephthalate MOF-templated synthesis of porous nano-crystalline Co_3O_4 by the new indirect solid state thermolysis as cathode material of asymmetric supercapacitor, Phys. E Low Dimens. Syst. Nanostruct. 94 (2017) 158–166.